Faraday
Discussions

Accepted Manuscript

Faraday Discussions

Royal Society of Chemistry

ROYAL SOCIETY
OF CHEMISTRY

ROYAL SOCIETY
OF CHEMISTRY

ROYAL SOCIETY
OF CHEMISTRY

Faraday Discussions

ARTICLE

Monitoring plasmon coupling and SERS enhancement through *in situ* nanoparticle spacing modulation

L. Velleman,†[a] L. Scarabelli,[b,d,e] D. Sikdar,[a] A. A. Kornyshev,[a] L. M. Liz-Marzán,[b,c] and J. B. Edel†[a]

Self-assembled nanoparticle (NP) arrays at liquid interfaces provide a unique optical response which has opened the door to new tuneable metamaterials and for sensing and optical applications. NPs can spontaneously assemble at the liquid-liquid interface, forming an ordered, self-healing, low-defect 2D film. The close proximity of the NPs at the interface results in collective plasmonic modes with a spectral response dependent on the distance between the NPs and induces large field enhancements within the gaps. In this study, we assembled spherical and rod-shaped gold NPs with the aim of improving our understanding of NP assembly processes at liquid interfaces, working towards finely controlling their structure and producing tailored optical and enhanced Raman signals. We systematically tuned the assembly and spacing between NPs through increasing or decreasing the degree of electrostatic screening between NPs with the addition of electrolyte or pH adjustment. The *in situ* modulation of nanoparticle positioning on the same sample allowed us to monitor plasmon coupling and the resulting SERS enhancement processes in real time, with sub-nm precision.

Introduction

The self-assembly of plasmonic NPs has long been recognised as a simple and efficient method to create NP arrays[1-3] and superstructures.[4-11] Plasmonic NPs are well known for their rich optical properties, highly dependent on their size, shape and composition. But their interaction, when confined in 2D or 3D structures, can vastly alter their optical properties due to the coupling of localized plasmon modes, revealing new collective plasmonic properties and enhanced Raman scattering originating from 'hotspots' – the areas of enhanced electromagnetic field near NPs and in the narrow gaps between them. By controlling not only NP size, shape and composition but also interparticle spacing, the plasmon resonance of the NP structure, density of hotspots and resulting Raman enhancement can be tailored at will.[12, 13]

The assembly of NPs at liquid interfaces, particularly liquid-air interfaces, has garnered much attention as a facile route to

forming 2D and 3D arrays of NPs over a macroscopic range.[14-17] These self-assembled films can be used *in situ* or further transferred onto solid substrates for use in a device. The assembly of NPs at liquid-liquid interfaces (LLI), while not as extensively studied as at liquid-air interfaces, offers a unique platform to study the collective plasmonic properties of NP arrays and their Raman scattering effects. Converse to liquid-air interfaces where drying forces the NPs together, at the LLI the NPs are more mobile and depending on assembly conditions the NPs can be kept further apart, thus accessing a greater range of interparticle spacings, from one nanometre to tens of nanometres. As the NPs at the LLI are encased between two liquid layers, conventional imaging techniques used to determine NP separation such as transmission and scanning electron microscopy (TEM & SEM), cannot be used *in situ*. Recently, other methods such as x-ray reflectivity and grazing-incidence small-angle x-ray scattering (GISAXS) have been employed for characterising the structure of buried NP films. With these techniques, we have previously shown inter-NP surface to surface spacing at the LLI to be easily tuned between upwards of 30 nm down to 4.5 nm.[18]

a. Department of Chemistry, Imperial College London, UK
b. Bionanoplasmonics Laboratory, CIC biomaGUNE, Paseo de Miramón 182, 20014 Donostia, San Sebastián, Spain
c. Ikerbasque, Basque Foundation for Science, 48013 Bilbao, Spain
d. California NanoSystems Institute, University of California, Los Angeles, Los Angeles, California 90095, USA
e. Department of Chemistry and Biochemistry, University of California, Los Angeles, Los Angeles, California 90095, USA
†l.velleman@imperial.ac.uk, joshua.edel@imperial.ac.uk.
Electronic Supplementary Information (ESI) available: [details of any supplementary information available should be included here]. See DOI: 10.1039/x0xx00000x

Faraday Discussions Accepted Manuscript
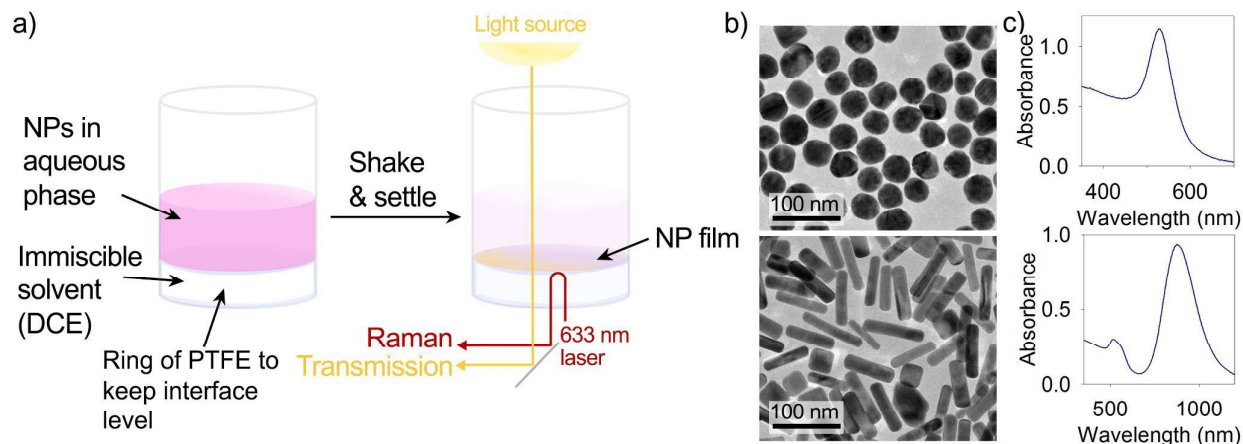
Figure 1 Schematics of NP film formation via emulsification of an aqueous solution of NPs with an immiscible solvent (DCE). The emulsified solution is allowed to settle leaving a 2D array of NPs at the liquid-liquid interface. The NP film is characterised with transmission spectroscopy to obtain the extinction spectra of the film and via Raman spectroscopy in inverted mode at a laser excitation of 633 nm. b) TEM images of a cast and dried solution of spherical GNPs (top) and GNRs (bottom). c) Corresponding absorbance spectra of as-prepared spherical GNP solution (top) displaying a single LSPR band at 527 nm and GNR solution (bottom) displaying two bands corresponding to the oscillation of the transverse (516 nm) and longitudinal (877 nm) plasmons.

In this study we have again exploited the self-assembly of NPs at LLI's to obtain highly ordered, self-healing, low-defect NP arrays, exploring the distance-dependent properties of both spherical and anisotropic gold NPs (Figure 1a). At the LLI NPs are mobile on the XY plane, rearranging themselves to minimise energy. Therefore, at equilibrium the distance between the NPs is optimised and defects such as voids and multi-layers are supressed. We systematically tuned the assembly and spacing between NPs through increasing or decreasing the electrostatic screening between the NPs. The *in situ* modulation of nanoparticle positioning on the same sample allowed us to monitor plasmon coupling and resulting surface enhanced Raman scattering (SERS) processes in real time with sub-nm precision. Previous studies on SERS at the LLI,[19-23] did not achieve control over ordering and interparticle spacing of the NPs at the interface, thereby resulting in varying Raman signals over the NP film. The main requirement for quantitative sensing applications is for a consistent SERS response over the SERS substrate, which only controlled order and spacing can provide. However it is a challenge to maintain such control whilst still remaining SERS active at the LLI. The organisation of NPs within the 2D assembly is highly dependent on the dimensions of the NP as well as the NP surface functionality and composition of the aqueous and organic phases. A fine balance is required for optimal self-assembly into an ordered array and becomes increasingly difficult to control for larger NPs (>20 nm).

This work highlights the ability to assemble large (>40 nm) spherical as well as anisotropic NPs (namely gold nanorods, GNRs), and exploiting the fluid nature of the LLI 'template' to manipulate NP spacing *in situ* with a fast response. We first present the assembly of 42 nm spherical gold nanoparticles (GNPs) (Figure 1b, top) where we focus on demonstrating the fluidity and dynamic response of the NP positioning when changing the surrounding NP environment. We then present the assembly of GNRs (78 x 17 nm, Figure 1b bottom) to demonstrate the versatility of this assembly procedure to be easily extended to shaped and surfactant-stabilised NPs. In particular, GNRs display two distinct plasmon resonance bands due to their anisotropic shape (Figure 1c). Anisotropy adds a new level of complexity to the self-assembly process, and the detailed study of optical changes derived from plasmon coupling between the different plasmon modes can lead to a better control over the process.[24-28] The highest electric field enhancement of GNRs is located at their tips[29, 30] and therefore a higher Raman signal is expected when the GNRs are arranged with small tip-tip gaps. However, until detailed analysis of the structural properties of GNRs at the interface is performed with x-ray reflectivity and GISAXS, we refrain from ascribing precise values of interparticle spacing for these films. Through exploring the assembly of NPs at the LLI we aim to further the understanding and improve techniques used to create the ordered, well-defined structures that are needed if these NP arrays are to become functional materials. These layers provide a unique opportunity to monitor optical and Raman scattering *in situ* as the interparticle spacing is changed and will help unlock the door to understanding short-range plasmon coupling and Raman enhancement processes of NPs in large arrays. Through programming NP size, shape, composition and spacing, these films can be fully tailored for their target application whether it be mirrors, filters, catalysts or sensors.

Results and discussion

NPs can adsorb at the interface between two immiscible liquids driven by the need to reduce the surface tension between the two liquids. However, there are several factors that determine whether the NPs will assemble and their order once at the interface. Firstly, the NPs are often stabilised by

charged ligands, brought about during their manufacturing process (eg. surfactants, sodium citrate, etc). No matter how much the NPs want to come to the interface to reduce the unfavourable surface tension, they must overcome their Coulombic repulsion in order to sit closely together. This can be achieved by "destabilising" the NPs.[31] In our case, we screen the charge of the ligands using an electrolyte, tetrabutylammonium tetraphenylborate (TBA TPB). However, there is a fine balance between destabilising the NPs so much that they simply flocculate at the interface, forming aggregates, and destabilising just enough that controlled assembly can take place at the interface. This fine balance is dependent on the surface functionalisation on the NPs, pH of the solution, the concentration of electrolyte and the presence of any other salts and stabilising compounds in the solution such as citrate ions and surfactants. In our case the surface of the NPs was functionalised with 4-mercaptobenzoic acid (4-MBA) as a Raman reporter, but functionalisation with either mercaptododecanoic acid (MDDA, in the case of spherical GNPs) or polyethylene glycol (PEG, in the case of GNRs) was also required to provide steric stability as 4-MBA alone is not enough to sufficiently prevent aggregation between the NPs during the assembly. Secondly, the diffusion time for the NPs in the bulk solution to reach the interface is slow. To speed this up the NP solution was emulsified with the organic solvent, whereby the distance for the NPs to reach the organic phase was drastically reduced. The two phases then separate out leaving an array of NPs at the interface.

Spherical GNPs were assembled at the LLI through emulsification of an aqueous solution of the GNPs containing 0.02 w/v% citrate with an immiscible organic phase, 1,2-dichloroethane (DCE) containing TBA TPB. Sodium citrate is a well-known NP stabiliser, used in GNP synthesis methods to stabilise and cap the growth of GNPs. For assembly at the LLI, citrate also plays a major role in the structure of the resulting GNP film. In our case, the amount of citrate needed to stabilise the GNPs just enough to produce a low-density monolayer was 0.02 w/v%, as indicated by a pink coloured film (Figure 2a). The absorbance spectrum of the solution of GNPs is shown in Figure 1c (top), displaying a localised surface plasmon resonance band (LSPR) at approximately 527 nm. As the GNPs come closer together (within 2.5 times the NP dimension) their plasmons couple, shifting the plasmon resonance to lower energy which is seen as a red-shift in the LSPR peak. In essence, we used this LSPR shift as a "plasmonic ruler"[32-35], whereby the position of the LSPR peak can be related to the gap distance between the NPs. The LSPR of GNPs assembled into the film shifted to 558 nm (Figure 2b). From our previous study,[18] the theoretical model was adapted to 42 nm GNPs and predicts an LSPR position of 558 nm to correspond to GNPs spaced 30 nm apart. It should be noted that the gap distances calculated are averages over the NP array. Further, as the extinction spectra are measured over a large area (1.33 mm field of view), the spectra are average representations of particle spacing spanning many NP domains. For instance, a domain size of ~142 nm for 13 nm GNPs was previously measured.[18] The stabilising effect of citrate ions was then

exploited to control the positioning of the GNPs relative to each other at the interface. The complete removal of citrate ions destabilises the GNPs, allowing them to move closer together: the film turns blue/purple in colour (Figure 2a) and the LSPR red-shifts to 675 nm (Figure 2b) which corresponds to an interparticle spacing of approximately 1.9 nm. At the same time a dramatic increase in the Raman signal was observed (Figure 2c), with the dominant peaks at 1080 and 1590 cm^{-1} rising from approximately 22 and 21 counts respectively to 908 and 1072 counts. The peaks at 1080 and 1590 cm^{-1} correspond to the υ_{12} and υ_{8a} aromatic ring vibrations from the adsorbed 4-MBA respectively.[36] A control Raman spectrum of an assembly of GNRs unmodified with 4-MBA shows that no other peaks occlude the dominant 4-MBA peaks at 1080 and 1590 cm^{-1} (ESI Figure 2). The SERS spectra display a few differing bands when the NPs are 30 and 1.9 nm apart. When the NPs are 30 nm apart the spectrum is dominated by peaks from the solvent, DCE (ESI Figure 2; e.g. at 1058, 1149 & 1300 cm^{-1}). As the NPs are brought closer together the 4-MBA peaks dominate. In addition to the main vibrational bands of 4-MBA at 1080 and 1590 cm^{-1}, peaks at 1180 & 1485 cm^{-1} arise, which are attributed to the δ_{CH} and $\gamma_{CH\text{-}as}$ vibration respectively.

The enhancement factor (EF) is calculated by;

$$\mathrm{EF} = \frac{I_{\mathrm{SERS}}\,N_{\mathrm{NRS}}}{I_{\mathrm{NRS}}\,N_{\mathrm{SERS}}} \qquad (1)$$

Where I_{SERS} and I_{NRS} represents the intensity of the Raman signal for 4-MBA on the SERS platform and for a bulk powder sample of 4-MBA respectively and N_{SERS} and N_{NRS} represents the number of 4-MBA molecules within the probe volume on the SERS platform and within the bulk powder sample. A detailed description of how the EFs are calculated can be found in the supporting information. The theoretical EFs based on $|E/E_0|^4$ calculations are plotted against GNP spacing in ESI Figure 5. The plot does not extend to GNPs spaced farther than 11 nm but based on literature the EF of GNPs spaced 30 nm apart would be similar to a single sphere at this distance, estimated to be around 1000.[37] The experimental EF for the film prepared with 30 nm interparticle spacing was calculated to be 4.3 x 10^4. We observe an overall larger EF in experimental values as the theoretical model takes into account only perfectly spherical NPs where in reality our NPs are faceted, containing sharp edges and tips where the electric field enhancement is increased,[37] and potentially a small degree of aggregation which could easily increase the average EF. The experimental EF at 1.9 nm (8.4 x 10^5) compares well with the theoretically derived value of 3.85 x 10^5. A closer look into the controlled manipulation of LSPR and EFs will be reported in a separate study.

The main finding we would like to convey in this study is the dynamic response of NP positioning that can be achieved at the LLI. The real-time modulation of NP spacing is a true benefit of working with NP layers at the LLI. By exploiting the freedom in movement of NPs at the LLI a variety of NP spacings can be accessed on the same sample and their repositioning can be rapid, limited only by the diffusion speed of molecules to the interface. To demonstrate this, we injected
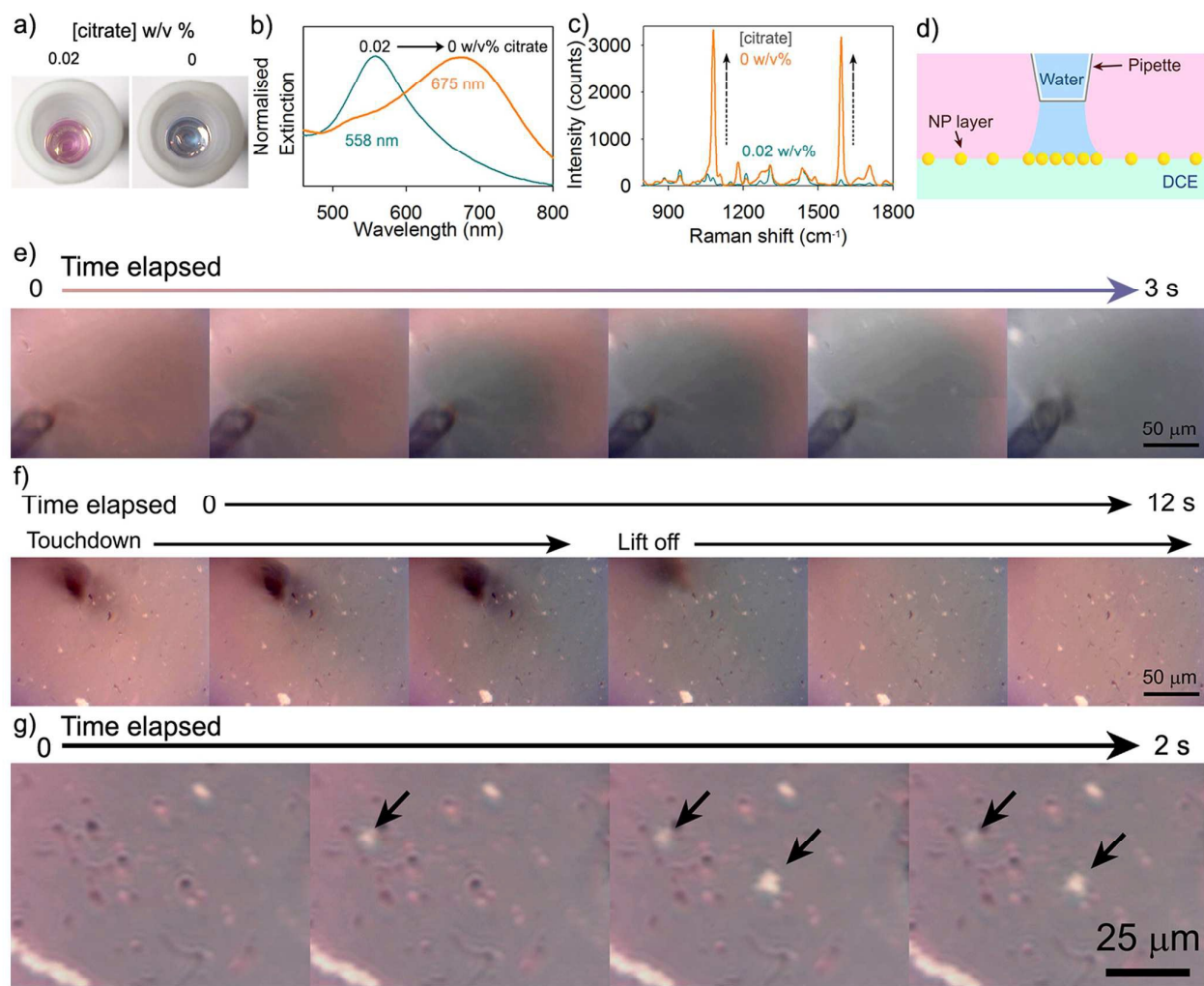
Figure 2 Assembly of spherical GNPs at the LLI by emulsification with 10 mM TBA TPB in the DCE phase and 0.02 % citrate added to the aqueous phase. The NPs were subsequently drawn closer together by reducing the citrate concentration from 0.02 to 0 w/v% by replacing the entire aqueous phase with water. a) Photographs of the GNP film taken from above, prepared at 0.02 w/v% citrate (left) and after reducing the citrate concentration to 0 w/v% (right). b) Extinction spectra of the original GNP film exhibiting an LSPR of 558 nm which is then red-shifted to 675 nm and broadened as the citrate is removed. c) Raman spectra of the NP film before and after reduction in citrate concentration. The peaks are from 4-mba adsorbed onto the surface of the NPs. d-f) Optical microscopy images extracted from a video as a micropipette was brought close to the NP film and water injected just above the layer using a syringe pump. d) As the water is pumped in above the GNP layer the film turns from a pink colour to blue/grey. The response is rapid, the images taken within a 3 s timeframe. e) Images displaying the self-healing properties of the film. The micropipette is lowered towards the interface the film which turns the film blue/grey. As the pipette is extracted away from the interface the film is seen to return to its original pink colour. f) Images showing the formation of voids in the film as the GNPs rearrange themselves into a closer packed order.

water through a micropipette positioned just above the NP interface, thereby diluting the local concentration of citrate ions and providing a localised region of pure water directly beneath the pipette (Figure 2d). Figure 2e presents a time-lapse series of optical microscopy images taken of the GNP film as the micropipette is lowered towards the interface. The videos can be found in the supporting information. In a span of 3 s the film is flooded with water and the film is seen to change colour from pink to blue/grey. Due to the absence or dilution of citrate ions within the region flooded with water, the NPs can move closer together. The blue-grey colour closely resembles the colour of the film after completely replacing the aqueous phase with water, as shown in Figure 2a-c and we can therefore expect a similar LSPR. While we are unable to measure the local optical spectra of the film as the spot size of our optical set up is up to ten times larger than the area

flooded, we are confident that the colour change observed presents a similar red-shift in the LSPR as seen in Figure 2b and hence a corresponding reduction in interparticle spacing.

The film is self-healing, once the pipette is lifted away from the interface citrate ions diffuse back to the layer and the film recovers its original appearance after several seconds, suggesting that the NPs have been pushed apart, close to their original spacing (Figure 2f). The response time in the rearrangement of NPs is limited only by the diffusion rate of water or citrate ions to the interface, which can be altered by flow rate and the distance of the outlet to the interface. For example, citrate solution can also be pumped into the interface to regenerate the layer more quickly.

If we assume that the NPs are ~1.9 nm apart while flooded with water, based on the control in Figure 2b, this would suggest that perhaps the NPs are in complete contact and

irreversibly attached as the ligand length of MDDA is ~ 1.5 nm. One reasoning could be that, as the monolayer is mixed and on a highly curved surface, the monolayer is expected to be disordered and may in fact be ≤ 1 nm thick. Alternatively, the thiol layers may compress together without becoming entwined. For the set of images in Figure 2f we performed analysis on the grey intensity to help quantify the local optical changes within the film (ESI Figure 4). Indeed, we do not observe full reversibility of the film within this timescale, the overall grey intensity of the film approaches but does not reach the film's initial intensity. Either, a small population of GNPs remain stuck together or the attractive forces once the NPs have come together are much stronger and require more citrate to push them farther apart. Perhaps, given time or an injection of citrate ions into the layer, or by not completely removing the stabilising citrate ions, the process can be made fully reversible.

The rearrangement of the film as the NPs assume a closer interparticle spacing is evident from small holes appearing in the film as water is injected (Figure 2g). With such a localised area where the NP spacing is altered, it could be possible to draw small circles or patterns dependent on the dimension of the micropipette or water outlet. There is potential to deliver analytes of interest directly to the interface in conjunction with bringing the NPs together, providing a confined small area for analysis.

To demonstrate the versatility of the LLI as a platform for NP assembly we also explored the assembly of GNRs. Their distance-dependent optical and SERS properties are particularly interesting as GNRs possess two distinct plasmon resonances and the electric field is greatly enhanced at the tips of the rods. Firstly, numerical simulations were performed to view the expected trend in optical and electric field enhancement properties as GNR spacing is varied (Figure 3).

The numerical simulations presented in this work were performed using CST Microwave Studio Suite®. The frequency domain FEM solver was used to obtain the optical response of GNRs when self-assembled to form a monolayer. Full details on extracting the simulation data can be found in the supporting information. The trend for the excitation of the transverse and longitudinal plasmon modes are shown separately in Figure 3 a and b, respectively. In both cases, the plasmon resonance red-shifts and broadens with decreasing interparticle gap. We assume that the GNRs approach each other with the equal tip-to-tip and side-side separations for simplicity, although in reality it is likely one gap may shrink more in comparison with the other. From literature, Discrete

Dipole Approximation (DDA) simulations examined the approach of GNRs in a tip-to-tip and side-to-side configuration separately.[24, 25] As GNR sides come closer together a blue-shift was evident for both transverse and longitudinal modes in the optical spectra. When the GNRs come closer aligned in a tip-to-tip fashion, the longitudinal mode is seen to red-shift while the transverse mode remains stationary.

To identify the hot-spots at a laser excitation wavelength of 633 nm, we calculated electric field distribution patterns along the plane passing through the centre of the GNRs in a unit cell (Figure 3c). The unit cell is highlighted by the red box in the top schematic and is repeated in both lateral dimensions to emulate a large monolayer of GNRs. As expected, the maximum electric field enhancement is found at the tips of the rods and very little enhancement is observed in the gaps between the sides of the rods even at small gap distances. The electric field enhancement factor E/E_0 at the junction between the tips of the rods is marked for each interparticle spacing and is later converted to a theoretical estimate of the SERS EF (calculated as $|E/E_0|^4$). The maximum theoretical EF is plotted against interparticle gap in Figure 3d and documented in Table 1. A steady increase in EF is observed when the spacing is reduced from 8 to 2 nm and as expected, the EF increases significantly once the spacing reaches 1 nm.[37]

The distance dependent optical and SERS properties of GNR films were then investigated (Figure 4). Here, we sought to have just enough GNRs to cover the interface without them packing too densely and aggregating. An estimate of the number of GNRs in the prepared solution was determined from UV-Vis by a procedure outlined by Scarabelli et al.[38] From this estimation and based on the interfacial area, an amount of GNRs could be calculated to provide a desired interfacial coverage. However, from TEM analysis our GNRs display a significant size dispersion (length; 78 ± 10 nm, width; 17 ± 3 nm) and a small percentage of other shaped NPs such as spheres and cubes, and so the calculated number of GNRs in the solution is taken to be a ballpark figure. Further, as the NPs can assemble on the walls of the vials the actual surface coverage at the interface will differ from the calculation. Therefore, to ensure complete monolayer coverage, GNR films

Table 1 Theoretical maximum EF for GNRs assembled into an array at varying interparticle gap

Gap (nm)	Theoretical maximum EF
1	1.14×10^6
2	4.67×10^4
4	5.15×10^3
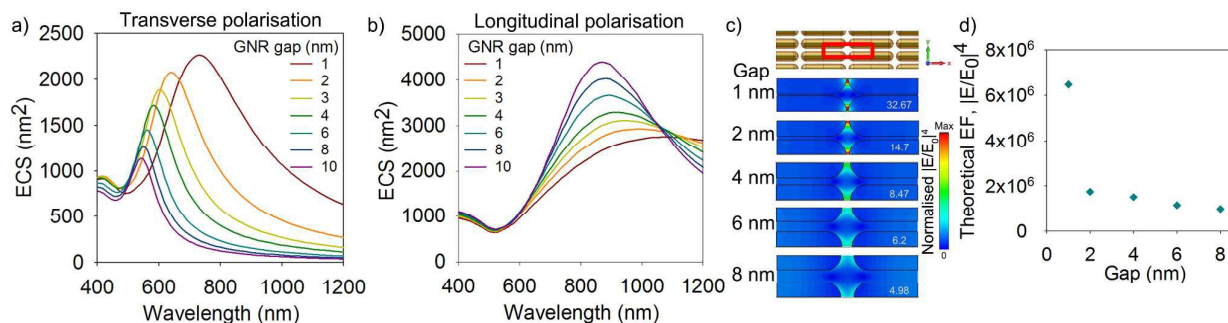
Figure 3 Theoretically calculated optical extinction spectra of a GNR film as a function of interparticle gap for transverse (a) and longitudinal polarisation (b). c) Simulation of 'hot-spots' in a monolayer of GNRs. The schematic of the simulation model is shown at the top, where the red rectangle highlights the unit cell that repeats periodically in both lateral directions to emulate a large monolayer of GNRs. Lower panels show the electric field distribution patterns that reveal the hot-spot formation for different gap spacings between the GNRs at excitation wavelength of 633 nm. The maximum value of the electric field enhancement factor is shown reight-bottom corner. d) Theoretical estimates for the maximum SERS EF, calculated as $|E/E_0|^4$, plotted as function of interparticle gap. Note that incident light is considered to propagate along z and polarized along x in all cases. The interparticle gaps in the monolayer, along the length and width of the GNRs, are considered to be equal in each simulation study.
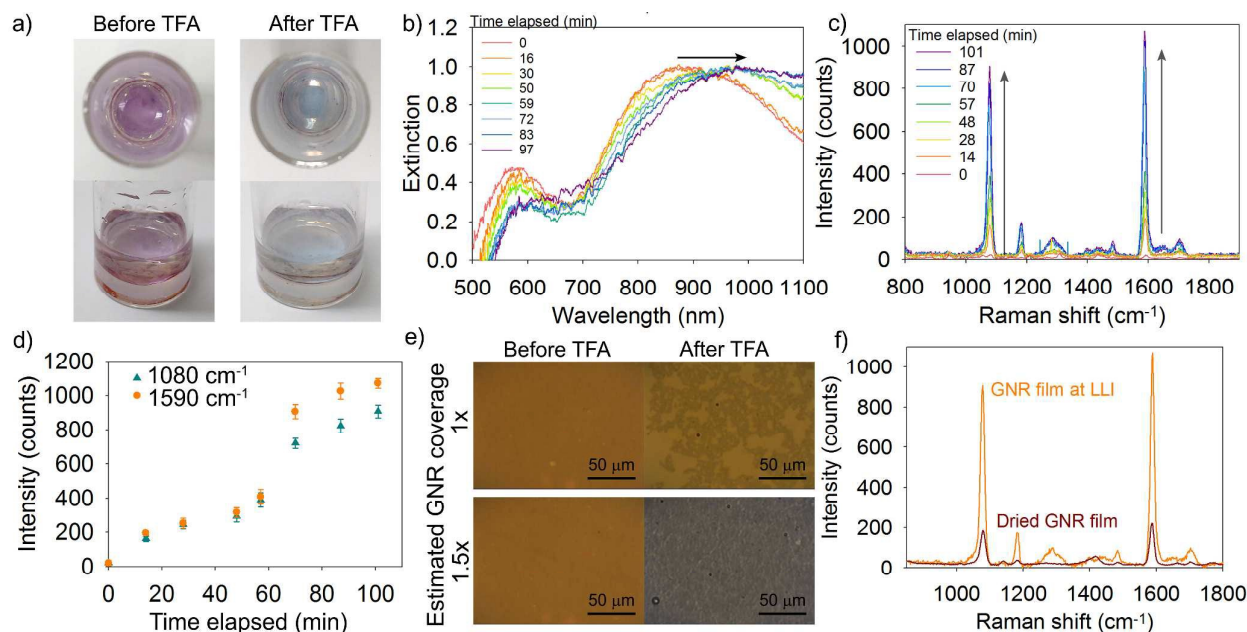
Figure 4 Assembly of GNRs into films at the LLI by emulsification with DCE containing 1 mM TBA TPB. The pH is lowered by adding 1 mM TFA to the DCE phase. a) Photos of the GNR film taken before and after TFA addition. The extinction (b) and Raman (c) spectra of the film is measured over the 100 min time period. Corresponding extinction and Raman spectra taken within a few minutes of each other are allocated the same colour in b) and c). Both transverse and longitudinal modes red-shift with time. The Raman intensity for the 4-mba peaks at 1080 and 1590 cm^{-1} increase steadily with time, and are plotted against elapsed time in d). e) Optical microscopy images of GNR films prepared at 1x and 1.5x surface coverage before and after TFA addition. f) Comparison of the Raman spectra of a close-packed GNR film formed at the LLI (t=101 min in timeseries) and the equivalent amount of GNRs/nm^2 dried onto a glass slide.

were made at 1 - 1.5x the interfacial surface area. The extinction spectra of these films can be found in ESI Figure 6. They each possess similar LSPR positions. However, the film prepared at 1.5x coverage appeared slightly more stable and well packed under optical microscopy and was therefore used in the subsequent study. In a sparsely packed film the layer appears to be more fluid and the movement of bubbles and defects can be observed. These films were not observed to contain multilayers under optical microscopy, implying that the actual surface coverage is below 1 x coverage.

Similar to the addition of electrolytes to screen the NP charge and bring them together, so too can changing the pH. In our case we used trifluoroacetic acid (TFA) to reduce the pH. An acidic environment will cause the adsorbed 4-MBA ligands to become protonated, reducing the repulsive forces between the GNRs. TFA is miscible in both the organic and aqueous phases and so we added TFA to the organic phase to allow slow diffusion across the interface so we could monitor the film changes over a longer period of time. When TFA is added to the aqueous phase the transition was rapid (changing colour by eye as soon as the TFA was added). The original pink/purple colour of the GNR film is seen to turn blue/grey upon TFA addition (Figure 4a). The extinction spectra of the film and the Raman spectrum of 4-MBA were monitored over a period of 100 min after TFA addition (Figure 4b and c). There is a time delay between the acquisition of the extinction and Raman spectra and therefore for ease of viewing, the spectra measured within a few minutes of each other are colour coded. As the transition in the film is relatively slow, the two measurements should correspond appropriately.

For clarification, we have normalised the extinction spectra to the longitudinal LSPR band to clearly observe the shift in the spectra over time. Both transverse and longitudinal LSPR modes are seen to red-shift over time. The prominence of the transverse mode also decreases over time, merging into the longitudinal LSPR mode after 97 min. The longitudinal mode is seen to red-shift from 883 nm into a broad peak beginning around 974 nm. The transverse mode red-shifts to a lesser extent, beginning around 578 nm and ending at ~588 nm. From the literature the position of the transverse mode is seen to either remain constant (in the case of tip-to-tip orientation) or blue-shift (in the case of side-to-side orientation).[24, 25] However, it should be recalled that we have a large amount of spherical impurities within our GNR sample which will also cause a red-shift in their LSPR as they come closer together. As their LSPR is positioned close to the GNR transverse LSPR they will contribute to the appearance of a red-shift in this band. The red-shift in the longitudinal LSPR band could suggest the GNRs are predominantly oriented in a tip-to-tip arrangement at the interface based on DDA-simulations.[25] However, random orientations of GNRs can also produce a red-shift in the longitudinal and transverse LSPR band.[26, 39] Within a disordered array tip-to-tip, tip-to-side and side-to-side interactions can occur. Both tip-to-tip and tip-to-side interactions will produce a red-shift in the longitudinal LSPR.[24] Due to the large size dispersion in our GNR solution (77.6 ± 10.0 nm and 17.3 ± 3.0 nm for length and width respectively) we are likely dealing with a random array of GNRs. A section of the GNR film was extracted for viewing under TEM by passing a TEM grid horizontally through the interface to provide an indication of the possible structure of the GNRs at the interface. However, as the GNR film is greatly disturbed by this process in addition to the drying effects once the film is extracted, the structure of the film seen under TEM will differ from the structure at the LLI. The dried film is seen to have no apparent order (ESI Figure 7). Just as the structure of spherical NP films are highly sensitive to additives (eg. citrate, Figure 2a), so too will GNR assembly. It is a matter of finding such a combination for GNRs that will allow a higher degree of control over the alignment of the rods and their spacing.

The Raman peak intensity of 4-MBA on the GNR surface increases drastically after TFA is added. Originally the υ_{12} and υ_{8a} aromatic ring vibration modes at 1080 and 1590 cm^{-1} are barely discernible, their intensities are 22 ± 15 and 21 ± 16 counts respectively, which then increase to a maximum of 908 ± 37 and 1072 ± 29 counts respectively. The 1080 and 1590 cm^{-1} peaks are plotted against elapsed time in Figure 4c, showing a steady increase in both peaks. A slight step is observed between ~60 and ~70 min. Within the extinction spectra the two curves are similar, but with a slight difference that the longitudinal LSPR band at 72 min is broader and the transverse LSPR band flattens out. Perhaps indicating at this stage that GNR tips come close together and their tip-to-tip interactions dominate, boosting the Raman signal. A conservative calculation of the EF based on the intensity of the 4-MBA signal at 1080 cm^{-1} is recorded in Table 2. The EF is seen to increase by 40 x over the course of the experiment.

The experimental EFs are of similar value to the GNR simulations of ~ 2 nm interparticle spacing. However, the simulation EFs reported are maximum EFs while our experimental values are average EFs. It is expected the maximum EF to be higher than the average EF. We do, however, find our experimental average EFs in line with the simulations performed by Solis *et al.* on random arrays of GNRs of comparable dimensions.[12] Our final average EF of 8.79 x 10^4 is of similar magnitude to the calculated average EF when GNRs are spaced 1 nm apart.

Based on the longitudinal LSPR band position in the simulations (Figure 3b) it would be tempting to suggest that our arrays begin with a spacing of around 8 nm and end close to 2 nm. However, when there are two plasmon bands, complex coupling and a GNR size dispersion involved, a "plasmonic ruler" approach to associate GNR spacing may produce misleading results. It is difficult to image the structure of buried interfaces using conventional techniques such as TEM and SEM as they require dried samples which invariably alters the resulting structure of the film. The most accurate method to determine NP structures at the LLI is x-ray reflectivity and GISAXS which will be carried out in future work. Regardless, there is strong evidence that the GNRs are indeed moving closer together. After TFA addition the macroscopic structure of the GNR film drastically changes (Figure 4e), even forming clustered islands. The change is more obvious when the original film is less dense as is the case with the sample made at 1x interfacial coverage. After TFA addition the dark patches of clustered GNRs are seen to span around 3/4 of the image. Further, broadening of the band is a clear indication of plasmon coupling and hence reduction of interparticle spacing. However, it should be noted that the LSPR can also shift and the Raman signal increase due to changes such as the vertical positioning of the NPs between the two liquids and a change in the dielectric medium surrounding the particles. Indeed, previous simulations have shown that the LSPR of the NP can shift greatly depending on where it is sitting between the two phases.[40] So too can the enhancement increase by an order of magnitude when

Table 2 Intensity of Raman signal at 1080 cm^{-1} and calculated enhancement factors for GNRs assembled at the LLI as a function of time after TFA addition to the DCE phase.

Time (min)	Intensity of 1080 cm^{-1} peak (counts)	EF
0	22 ± 15	2.15 x 10^3
14	162 ± 15	1.57 x 10^4
28	244 ± 23	2.37 x 10^4
48	292 ± 32	2.83 x 10^4
57	391 ± 42	3.78 x 10^4
70	720 ± 30	6.97 x 10^4
87	823 ± 40	7.97 x 10^4
101	908 ± 37	8.79 x 10^4

ARTICLE

immersed in oil in comparison to the water phase. However, the study chooses a large difference in dielectric constant to maximise their observations, 1.77 and 5 for water and oil respectively. In our case the dielectric permittivity of the oil phase (DCE) is not that different from water: 2.08. Further simulations show the EF and extinction cross sections do not change greatly whether the GNRs are sitting fully in water or DCE (ESI Figure 8). In fact, for a 2 nm interparticle spacing the EF is calculated to decrease slightly from 4.67×10^4 for water to 2.95×10^4 in DCE and for 1 nm it increases very slightly from 1.14×10^6 in water to 1.21×10^6 in DCE.

The movement of NPs into the organic phase could also be of benefit. For example, if an organic phase is chosen which exhibits a larger SERS enhancement than water then the enhancement can be increased further. While the GNR data here is presented as preliminary work, it is of great importance to gain a stronger insight into the structure of the interfacial film, preferably through x-ray reflectivity which can provide the vertical positioning of the GNRs in respects to the interface, and GISAX which can characterise the interparticle spacing.

Finally, to highlight that the LLI is advantageous in the formation of NP arrays for SERS, we take a GNR film prepared at the LLI and compare its SERS response to a dried GNR film (Figure 4f). In the case of the dried film it was prepared by drop casting a solution of GNRs equivalent to the number of GNRs/nm^2 of the interfacial film. The SERS spectra shown are averages over a 20 μm area and 121 spectra. The SERS spectra present a few differing bands depending on whether the film is dried or interfacial. This is likely due to the absence of DCE peaks and a change in the molecular orientation of the 4-MBA after drying. The higher SERS intensity in the case of the GNRs formed at the LLI may suggest this layer is more ordered and maintains a higher density of ≥ 1 nm interparticle spacing for maximum hotspots whereas the lower signal for dried GNRs infer less hotspots likely from GNRs coalescing to < 1 nm gaps once dried, where SERS enhancement is lost to quantum tunnelling effects. It is also likely that the dried GNR film is more inhomogeneous, with large patches of GNRs forming rather than a smooth film. And although five areas were mapped, those areas tended to be lower density than the film formed at the LLI. Therefore, if an area of high GNR density could be located, the maximum EF for the dried film may reach the same magnitude as an interfacial film, but the average EF over the surface is lower due to inhomogeneity. Regardless, this again highlights the advantage of NP self-assembly at LLI's to prepare homogeneous films spanning large areas for a consistent average EF. Furthermore, the GNR film at the LLI was far quicker to prepare than even the dried film.

Concluding remarks

In this study, we have demonstrated that the LLI is a particularly useful tool for assembling NPs and monitoring their optical and Raman enhancement properties *in situ* and in real time. The dynamic response of the NP positioning at the interface was demonstrated for both spherical GNPs and GNRs.

Through removal of the citrate stabiliser in the aqueous phase we were able to decrease GNP spacing from 30 nm to 1.9 nm, with a concurrent significant increase in Raman signal of the 4-MBA Raman reporter, by almost 20 times. Changes in the NP spacing occurred rapidly over a timeframe of a few seconds and the film was able to self-heal, returning almost to its original appearance once citrate ions were allowed to diffuse back to the film.

GNR assemblies provided an interesting system to study due to their two plasmon modes and the localised enhancement at their tips. GNR films were exposed to a low pH environment to decrease the spacing between the particles. Both transverse and longitudinal LSPR modes red-shifted over time concurrent with a 40 times increase in the SERS signal. While it is possible to say that the GNRs are moving closer together, future work will need to include x-ray reflectivity and GISAXS measurements, polarised light experiments and *in situ* imaging to validate the structure of the GNR layer at the interface. Future experiments could also include further analysis into quantifying the response rate of the transitions. A GNR sample containing a narrower size dispersion and lower amounts of other shaped NPs will also benefit when interpreting the optical and Raman responses from such films.

Experimental

Materials

Gold (III) chloride (≥99.9%, HAuCl$_4$), sodium citrate, 4-MBA, mercaptododecanoic acid (MDDA), poly(ethylene glycol) methyl ether thiol (M$_n$ 6000), sodium borohydride, hexadecyltrimethylammonium bromide (CTAB, BioUltra ≥ 99.0%), hydroxylamine hydrochloride, silver nitrate (99.9999%), and L-ascorbic acid were purchased from Sigma-Aldrich and used as received. 1,2-Dichloroethane (DCE, 99%) was purchased from Sigma-Aldrich and neutralised by swirling the DCE with small amount of sodium carbonate powder and filtering through a 100 nm porous alumina membrane. Hydrochloric acid, nitric acid, ethanol, sodium bicarbonate and sodium hydroxide were purchased from VWR International.

Nanoparticle fabrication

All glassware used was thoroughly rinsed with acetone, ethanol, detergent and aqua regia (3:1 ratio of hydrochloric:nitric acid), then rinsed in sodium bicarbonate solution and water.

Spherical gold NPs were synthesized using a procedure described by Brown et al.[41] Firstly, 16 nm seed nanoparticles were synthesised via the Frens method.[42] A 500 mL solution of 0.1 w/v% gold (III) chloride was brought to boil under reflux with stirring. Once the solution began to boil, 10 mL of 1 w/v% sodium citrate was added and the reaction was allowed to proceed over 30 min then cooled to room temperature and filtered through a 0.2 μm mixed cellulose ester membrane (Advantec). For the growth of 42 nm gold NPs (TEM image, Figure 1b), 60 mL of the 16 nm gold seed was added to 540 mL milli Q water. Under vigorous stirring 6 mL of 0.2 M

hydroxylamine hydrochloride was added, stirred for 1 min then 5 mL of 1 w/v % $HAuCl_4$ solution was added. For modification of the NP surface with thiols the pH of the solution was adjusted to 7 through the addition of 1.6 mL 1 M sodium hydroxide. 10 mM solutions of 4-MBA and MDDA were made in ethanol and mixed in a ratio of 80:20 MBA:MDDA to which 612 μL of this solution was added to the GNPs and left to functionalise for 15 h. The GNPs were centrifuged at 3000 rpm for 1 h and resuspended in MilliQ water. All NP solutions were filtered through a 0.2 μm mixed cellulose ester membrane (Advantec) and stored in dark at 4°C.

GNRs were synthesized by the procedure outlined by Scarabelli et al.[38] To prepare the seed solution 25 μL 50 mM $HAuCl_4$ was added to 4.7 mL solution of 100 mM CTAB at 27°C under stirring. 5 min later 300 μL 10 mM sodium borohydride was added and the seeds were left to sit for 30 min. To grow the GNRs, 1 L solution of 100 mM CTAB in a flask was heated to 27°C in a water bath under stirring. 10 mL of a 50 mM solution of $HAuCl_4$ and 19 mL 1 M HCl was added to the flask. After 5 min had passed 12 mL of a 10 mM $AgNO_3$ solution was added followed by 8 mL of a 100 mM ascorbic acid solution. After the solution turned colourless 2.4 mL of the seed was added, stirred for 30 s then stopped and allowed to sit for > 15 h. The GNRs were centrifuged three times in total, twice at 7000 rpm for 25 min, resuspending in water then 0.5 mM CTAB. The GNRs were then functionalised with PEG by using a simple geometrical/stoichiometric calculation to estimate the amount of gold surface available[38] and then adding an amount of PEG equivalent to ~ 2x PEG molecules/nm^2. After 25 min a solution of 4-MBA in ethanol was added to the GNRs at a concentration equivalent to ~ 17x 4-MBA molecules/nm^2. The functionalised GNRs were centrifuged 24 h later at 6000 rpm for 30 min and re-suspended in 0.5 mM CTAB.

Assembly of gold NP layers at the liquid-liquid interface

NP layers were assembled in custom made glass vials of 17 mm internal diameter, 12 cm in height, with an optically flat base. A thin ring of PTFE of ~ 4 mm in height was placed at the bottom of each vial to allow a flat interface to form between the aqueous and organic phase. 3 mL TBA TPB containing DCE was added to the vial followed by the addition of the NP solution.

The vial was then capped with a glass stopper and vortexed at maximum speed for 1 min. During vortexing an emulsion between the organic and aqueous phase forms thereby allowing short distances for the NPs to travel to the interface and assemble. The two phases generally separate out within a minute and the NPs will arrange themselves at the flat LLI. A 2.5 mL glass syringe (Hamilton), with flat 22 gauge needle, was used to remove any small bubbles of trapped NP solution from the bottom of the glass vial. Excess DCE was extracted to bring the interface in line with the top of the PTFE ring, providing a flat interface.

A 1 mL sample of the aqueous phase was taken for UV-Vis analysis to determine how many NPs were depleted from the bulk and provide an estimate of the amount assembled at the interface. For assembly of spherical GNPs the aqueous phase

consisted of 3.12×10^{11} gold NPs/L (equivalent to an estimated 3 x interface coverage), and 0.02 w/v % citrate made up to a total volume of 8 mL. The organic phase consisted of 10 mM TBA TPB in DCE. For GNR film assembly, enough GNRs were added for an estimated 1.5 x interface coverage then made up to 5 mL with MilliQ water. The DCE phase consisted of 1 mM TBA TPB. After vortexing, the aqueous phase was replaced with 0.5 mM CTAB to maintain GNR stability.

Characterisation

UV-Vis and Vis-NIR absorbance spectra of NP solutions was carried out on a Nanodrop 3000 and a Shimadzu 2600 spectrophotometer respectively.

TEM analysis of NPs was carried out on a JEOL 2100 Plus.

Raman measurements were performed on a home-built Raman microscope. The instrument is based on an optical inverted microscope (IX71, Olympus) connected to a spectrograph (Shamrock SR-303i, Andor) fitted with an electron-multiplying charge-coupled device (CCD, Newton DU970BV, Andor). A 632.8 nm HeNe laser (HRP170, Thorlabs, 21 mW) excitation source was used. A 20x long working distance objective (LCPLFLN-LCD, Olympus) was fitted in order to reach the interface. A laser intensity of 380 μW, 50 μm slit width, and 600 l/mm grating was used for all measurements. The laser was focused onto the interface by finding the maximum Raman signal when traversing the z-direction through the layer. Raman spectra for spherical GNP films were acquired using a 5 s exposure time over 30 separate areas on the interface and averaged. Raman spectra for GNR films were acquired at an integration time of 1 s and averaged over 10 spectra.

Extinction spectra of the interfacial NP films was carried out on the same home built Raman spectrometer. Light from a Tungsten-Halogen light source (SLS202L,Thorlabs) was directed through a 105 μm optical fibre to a collimator and passed perpendicularly through the NP interface. For spherical GNP films a 633 nm collimator was used (F260FC-B, Thorlabs) and for GNR films a 850 nm collimator was used (F280FC, Thorlabs). The transmitted light was collected with the 20x long working distance objective then focused into the spectrograph. A 150 l/mm grating was used in all cases.

For spherical GNPs all spectra were acquired using the Newton DU970BV CCD, a slit width of 1 mm, 50 ms exposure time, and averaged over 100 scans at 5 different points on the sample. For GNR films all spectra were acquired using an iDus490 InGaAs detector (Andor), 200 μm slit width and 5 s exposure time.

Acknowledgements

References

1.   A. Tao, P. Sinsermsuksakul and P. Yang, *Nat Nano*, 2007, **2**, 435-440.

2.   M. K. Bera, H. Chan, D. F. Moyano, H. Yu, S. Tatur, D. Amoanu, W. Bu, V. M. Rotello, M. Meron, P. Král, B. Lin and M. L. Schlossman, *Nano Letters*, 2014, DOI: 10.1021/nl502450j.

3.   K. J. Si, D. Sikdar, Y. Chen, F. Eftekhari, Z. Xu, Y. Tang, W. Xiong, P. Guo, S. Zhang, Y. Lu, Q. Bao, W. Zhu, M. Premaratne and W. Cheng, *ACS Nano*, 2014, **8**, 11086-11093.

4.   L. Scarabelli, C. Hamon and L. M. Liz-Marzán, *Chemistry of Materials*, 2017, **29**, 15-25.

5.   C. Hamon, M. N. Sanz-Ortiz, E. Modin, E. H. Hill, L. Scarabelli, A. Chuvilin and L. M. Liz-Marzan, *Nanoscale*, 2016, **8**, 7914-7922.

6.   C. Hamon, S. M. Novikov, L. Scarabelli, D. M. Solís, T. Altantzis, S. Bals, J. M. Taboada, F. Obelleiro and L. M. Liz-Marzán, *ACS Photonics*, 2015, **2**, 1482-1488.

7.   C. Hamon, S. Novikov, L. Scarabelli, L. Basabe-Desmonts and L. M. Liz-Marzán, *ACS Nano*, 2014, **8**, 10694-10703.

8.   V. A. Turek, Y. Francescato, P. Cadinu, C. R. Crick, L. Elliott, Y. Chen, V. Urland, A. P. Ivanov, L. Velleman, M. Hong, R. Vilar, S. A. Maier, V. Giannini and J. B. Edel, *ACS Photonics*, 2015, **3**, 35–42.

9.   Y. Tian, T. Wang, W. Liu, H. L. Xin, H. Li, Y. Ke, W. M. Shih and O. Gang, *Nat Nano*, 2015, **10**, 637-644.

10.   R. J. Macfarlane, B. Lee, M. R. Jones, N. Harris, G. C. Schatz and C. A. Mirkin, *Science*, 2011, **334**, 204-208.

11.   A. Kuzyk, R. Schreiber, Z. Fan, G. Pardatscher, E.-M. Roller, A. Hogele, F. C. Simmel, A. O. Govorov and T. Liedl, *Nature*, 2012, **483**, 311-314.

12.   D. M. Solís, J. M. Taboada, F. Obelleiro, L. M. Liz-Marzán and F. J. García de Abajo, *ACS Photonics*, 2017, **4**, 329-337.

13.   J. B. Edel, A. A. Kornyshev, A. R. Kucernak and M. Urbakh, *Chemical Society Reviews*, 2016, DOI: 10.1039/C5CS00576K.

14.   A. Dong, J. Chen, P. M. Vora, J. M. Kikkawa and C. B. Murray, *Nature*, 2010, **466**, 474-477.

15.   A. B. Serrano-Montes, D. J. de Aberasturi, J. Langer, J. J. Giner-Casares, L. Scarabelli, A. Herrero and L. M. Liz-Marzán, *Langmuir*, 2015, **31**, 9205-9213.

16.   J. J. Giner-Casares and J. Reguera, *Nanoscale*, 2016, **8**, 16589-16595.

17.   Q. Shi, K. J. Si, D. Sikdar, L. W. Yap, M. Premaratne and W. Cheng, *ACS Nano*, 2016, **10**, 967-976.

18.   L. Velleman, D. Sikdar, V. Turek, A. Kucernak, S. J. Roser, A. A. Kornyshev and J. Edel, *Nanoscale*, 2016, **8**, 19229-19241.

19.   M. P. Cecchini, V. A. Turek, A. Demetriadou, G. Britovsek, T. Welton, A. A. Kornyshev, J. D. E. T. Wilton-Ely and J. B. Edel, *Advanced Optical Materials*, 2014, **2**, 966-977.

20.   Y. Xu, M. P. Konrad, W. W. Y. Lee, Z. Ye and S. E. J. Bell, *Nano Letters*, 2016, **16**, 5255-5260.

21.   K. Kim, H. S. Han, I. Choi, C. Lee, S. Hong, S.-H. Suh, L. P. Lee and T. Kang, *Nat Commun*, 2013, **4**.

22.   S. G. Booth, D. P. Cowcher, R. Goodacre and R. A. W. Dryfe, *Chemical Communications*, 2014, **50**, 4482-4484.

23.   M. P. Cecchini, V. A. Turek, J. Paget, A. A. Kornyshev and J. B. Edel, *Nature Mater.*, 2013, **12**, 165-171.

24.   P. K. Jain, S. Eustis and M. A. El-Sayed, *The Journal of Physical Chemistry B*, 2006, **110**, 18243-18253.

25.   M. Gluodenis and C. A. Foss, *The Journal of Physical Chemistry B*, 2002, **106**, 9484-9489.

26.   S. Vial, I. Pastoriza-Santos, J. Pérez-Juste and L. M. Liz-Marzán, *Langmuir*, 2007, **23**, 4606-4611.

27.   Y. Bao, L. Vigderman, E. R. Zubarev and C. Jiang, *Langmuir*, 2012, **28**, 923-930.

28.   M. J. A. Hore and R. J. Composto, *ACS Nano*, 2010, **4**, 6941-6949.

29.   J. Kumar and K. G. Thomas, *The Journal of Physical Chemistry Letters*, 2011, **2**, 610-615.

30.   T. Chen, C. Du, L. H. Tan, Z. Shen and H. Chen, *Nanoscale*, 2011, **3**, 1575-1581.

31.   M. E. Flatte, A. A. Kornyshev and M. Urbakh, *J Phys Chem C*, 2010, **114**, 1735-1747.

32.   P. K. Jain and M. A. El-Sayed, *Chemical Physics Letters*, 2010, **487**, 153-164.

33.   K. H. Su, Q. H. Wei, X. Zhang, J. J. Mock, D. R. Smith and S. Schultz, *Nano Letters*, 2003, **3**, 1087-1090.

34.   P. K. Jain, W. Huang and M. A. El-Sayed, *Nano Letters*, 2007, **7**, 2080-2088.

35.   V. A. Turek, M. P. Cecchini, J. Paget, A. R. Kucernak, A. A. Kornyshev and J. B. Edel, *ACS Nano*, 2012, **6**, 7789-7799.

36.   D. W. Mayo, F. A. Miller and R. W. Hannah, *Course notes on the interpretation of infrared and Raman spectra*, John Wiley & Sons, 2004.

37.   E. C. Le Ru and P. G. Etchegoin, *Principles of Surface-Enhanced Raman Spectroscopy*, Elsevier, Amsterdam, 2009.

38.   L. Scarabelli, A. Sánchez-Iglesias, J. Pérez-Juste and L. M. Liz-Marzán, *The Journal of Physical Chemistry Letters*, 2015, **6**, 4270-4279.

39.   X. Hu, W. Cheng, T. Wang, Y. Wang, E. Wang and S. Dong, *The Journal of Physical Chemistry B*, 2005, **109**, 19385-19389.

40.   Z. Yang, S. Chen, P. Fang, B. Ren, H. H. Girault and Z. Tian, *Physical Chemistry Chemical Physics*, 2013, **15**, 5374-5378.

41.   K. R. Brown, D. G. Walter and M. J. Natan, *Chemistry of Materials*, 2000, **12**, 306-313.

42.   G. Frens, *Nature*, 1973, **241**, 20-22.

Faraday Discussions Accepted Manuscript